Airborne soiling measurements of entire solar fields with Qfly

Cite as: AIP Conference Proceedings **2303**, 100008 (2020); https://doi.org/10.1063/5.0028968
Published Online: 11 December 2020

Fabian Wolfertstetter, Robin Fonk, Christoph Prahl, Marc Röger, Stefan Wilbert, and Jesús Fernández-Reche

Airborne Soiling Measurements of Entire Solar Fields with Qfly

Fabian Wolfertstetter[1,a)], Robin Fonk[1], Christoph Prahl[1], Marc Röger[1], Stefan Wilbert[1] and Jesús Fernández-Reche[2]

[1]*DLR, Institute of Solar Research, 04200 Tabernas, SPAIN*
[2]*CIEMAT, Solar Concentrating Systems Unit, Plataforma Solar de Almería, 04200 Tabernas, SPAIN*

[a)]Corresponding author: fabian.wolfertstetter@dlr.de

Abstract. Concentrating Solar Power (CSP) plants are often being built in regions with high dust loads such as the Middle East and North Africa. Current soiling measurement methods in solar fields are labor and cost intensive and they only cover small measurement spots. Even a high number of manual measurements can only cover a minimal portion of the total solar field mirror surface. Airborne measurement solutions such as QFly have been developed in recent years to measure the geometry and tracking accuracy of the large CSP mirror areas. Soiling on solar mirrors is qualitatively visible in raw QFly measurement images. In this study we present a method to automatically derive the mirror cleanliness from aerial images taken with QFly. We present scattering investigations that correct for the directional particle scattering, illumination and camera viewing angles. A promising correlation was found between the thus corrected camera RGB signals and reference reflectance measurements that shows an RMSD of 3% for the investigated dust.

INTRODUCTION

Knowledge of the average soiling level of a solar field is necessary for power plant operators to schedule cleaning activities within a solar field and predict the power plant output with better accuracy [1, 2]. Current soiling monitoring methods applied in solar fields are either performed continuously on mirror samples that are exposed next to the actual collectors [3], or handheld reflectometers are employed that only measure tiny spots on a number of selected mirror facets [4]. The reflectometer method is expensive as it requires significant amounts of manpower if sufficient data for a representative average reflectance for the entire solar field needs to be determined [5, 6].
Camera based methods for soiling detection have been presented before: [7] developed a method to characterize heliostat reflectance in tower power plants. The method uses an illuminated Lambertian target on the solar tower whose reflected image as seen in the heliostat by a camera on top of the tower is analyzed. The difference of reflected and direct images of the lambertian target is used to derive the reflectance of the heliostat mirror facets. The method has been tested in a laboratory experiment.
Another study categorized the mirror surface by a number of thresholds for camera grey values into several intensity bins. The number of pixels showing the mirror suface with low RGB signal is compared to reference reflectance measurements taken on the lab sized mirror samples. A rough correlation is found. The authors suggest to use a dark background and compare different camera RGB channels in order to get the best results. [8]

In this study we present a novel measurement method to derive spatially resolved information on the soiling level over the entire solar field of a parabolic trough solar power plant. The method uses an unmanned aerial vehicle (UAV) to carry a high resolution camera over the solar field. The method separates the contribution of light scattered at dust particles from the other influences on the camera signal such as . From the scattering information, the cleanliness can be derived if the scattering behaviour of soiling layers, the lighting conditions at the moment of measurement as well as the positions of camera, mirror, sun and absorber tube are known. Much of this information can be derived directly from the existing QFly algorithms available at DLR [9]. The new method makes use of sun position and scattering simulations in order to increase its measurement accuracy.

SolarPACES 2019
AIP Conf. Proc. 2303, 100008-1–100008-10; https://doi.org/10.1063/5.0028968
Published by AIP Publishing. 978-0-7354-4037-1/$30.00

In the first part of this study we present a proof of principle measurement campaign that was conducted at PSA. The second part identifies the influencing factors on the camera signal and their relevance for the method. Correction functions are presented and applied to the measurement that include scattering simulations and viewing angle considerations. Finally, the application of the correction functions to the raw measurement is presented.

DESCRIPTION OF MEASUREMENT CAMPAIGN

During a QFly measurement at PSA, a dataset for the testing of the presented method has been acquired. The KONTAS collector [10] at Plataforma Solar de Almería (PSA) has been left to soil during eight weeks prior to the measurements. On a sunny day with a few cirrus clouds, an UAV flight was performed taking pictures of the collector from different angles during the flight that followed a spiral route above the collector during 10 minutes. After the UAV flight, reference reflectance measurements were taken with a Devices & Services R15 handheld reflectometer [11] at 20 spots distributed about the lower half of the collector surface. The reflectance measurements were registered and the location of measurement on the mirror was detected. The accuracy of the measurement location can be estimated to be 3 - 5 cm. The handheld reflectometer employed here has a measurement accuracy of around 1% [4].

In a first evaluation approach, only those measurement spots located in areas of the mirror where the black absorber tube (HCE) is reflected were taken into account. A raw picture and the Region of Interest (ROI) are schematically shown in Fig. 1. The raw UAV pictures are then processed by parts of the QFly software package. First, an orthogonalization is performed. The region of the direct HCE reflection is automatically derived from the existing QFly software package together with the location of the drone, the position and orientation of the collector surface, the HCE position and the sun position.

The locations of the reference measurements are then mapped on the orthoimages for evaluation. At these measurement spots, the image RGB counts are averaged channelwise over an area of 5 x 5 pixels (approximately 2 x 2 cm^2 on the mirror) and saved together with their corresponding reflectance for each picture.

If we compare the reference reflectance with the camera grey values from different camera pictures, a rough correlation is found between the two parameters, see Fig. 8 a). This suggests, that the brightness of the measurement spot is roughly proportional to the reflectance value at same mirror spots. This can be understood considering that particles constituting the soiling layer on a solar mirror scatter a portion of incident light depending on their optical properties (size, shape, refractive index). The more particles are deposited per unit mirror surface, the more light is scattered if constant illumination conditions are assumed. A portion of the scattered light will be directed towards the UAV camera and thus contribute to the pixel RGB value depicting the mirror area in question and make it appear brighter than a spot with less or no particles. This is especially valid if the background is relatively dark such that the additional contribution by the soiling particles can be resolved by the camera. Therefore we analyse the mirror area showing the reflection of the black absorber tube for this method. With background we mean the images of objects that are directly reflected in the mirror spot in question.

ANALYSIS OF CONTRIBUTION TO THE CAMERA SIGNAL AND EVALUATION METHOD

We could see a clear correlation between the camera grey values and the specular reflectance of solar mirrors, but to increase the accuracy and robustness of the method, various influence factors on the RGB signal can be considered. The camera's RGB signal is influenced by the background signal, the illumination conditions, the camera properties and the scattering and absorption of the actual soiling layer that we want to extract from the camera signal. We will analyze the influence of all three parameters in the following subsections before explaining the resulting evaluation procedure.

Influence of Background Radiation

The background image has to be subtracted pixelwise from the image reflected in a soiled mirror facet. The remaining portion of the camera grey value is caused by scattering at the soiling layer. From this contribution, the cleanliness can be derived. The region of the HCE reflected image is investigated in this study because it appears dark and thus contributes a comparably low share to the RGB signal. For the here presented version of the method, collectors in a solar field can not be measured during operation because the absorber tube will appear too bright. In this case

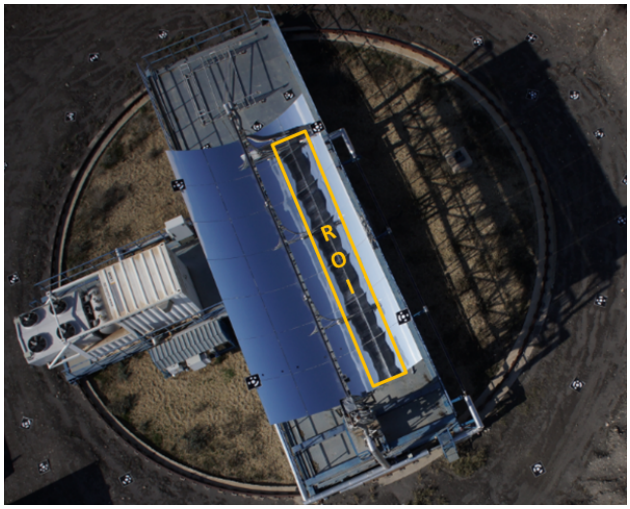

FIGURE 1. One of the raw pictures as taken with the UAV. Only points inside the region of the HCE's direct reflex, indicated by the orange rectangular ("ROI") are used for data evaluation.

mirror regions that do not show the reflected image of the HCE, but that of the sky or clouds could be analyzed. The background contribution would be generally higher and more inhomogeneous. If these regions should be analyzed, the background would have to be determined separately e.g. by a sky luminance model as described in [12]. Alternatively, an all sky imager such as [13] could be used to measure sky luminance directly and include it in the evaluation algorithms. The limitation to the mirror areas where the direct reflection of the tube appears is not significant because an extensive amount of pictures can be taken during a drone flight and evaluated automatically. The analyzable region will thus swipe all the mirrors below the flight trajectory.
The background will contribute to the radiant flux incident on a camera pixel following

$$\Phi_{px}^{back} = \rho_{mirr} \cdot \int_{A_{Px_{cam}}} \int_{\Omega_{Px}} L_{back}\, dA\, d\Omega \tag{1}$$

where L_{tube} is the radiance distribution function of the background, here describing light coming from the absorber tube. $A_{Px_{cam}}$ is the area of one pixel at the plane of object and Ω_{Px} is the solid angle defined by the camera position and the area of the absorber tube that is visible in the pixel. ρ_{mirr} is the clean reflectance of the mirror.

Scattering at the Soiling Layer

Given the size range of particles deposited on a mirror [14] and the visible part of the solar spectrum detected by a RGB camera, the Mie-Theory is used to solve the Maxwell equations. If a radiance L is incident on a spherical particle, the scattered radiance $L(\theta,\varphi)$, given in $W/m^2/sr$ in all directions θ and φ can be described by the Mie-Theory via the phase function $P(\theta,\varphi)$. $P(\theta,\varphi)$ has no physical dimension, and its integral over all directions is 1:

$$\int_0^{2\pi} \int_0^{\pi} P(\theta,\varphi) sin(\theta) d\theta d\varphi = 1 \tag{2}$$

The phase function can be thought of as a probability density function showing the chances of a photon being scattered in a specific direction. An example phase function is depicted in blue color in Figure 2 a [15, 16]. For spherical particles the phase function is symmetric around the direction of incident light and the angle θ is measured relative to this vector originating at the center of the particle.

On a solar mirror, four different contributions have to be considered for the calculation of the radiance scattered in the direction of the camera. First, the scattering contributions from a particle illuminated directly by the incident light sun_I is calculated, see Figure 3 a. Here sun_I is the vector from the particle to the sun position (red line), i.e. the direction of incidence. The vector from the scattering origin directly to the camera position, cam_I is shown as a black line and the vector from the particle over the mirror to the camera, cam_II, is shown as a black dashed line. This means

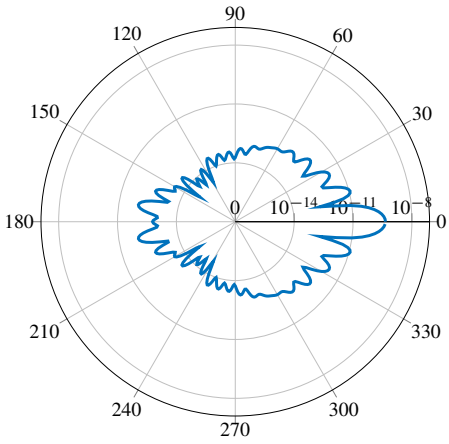

FIGURE 2. Scattered radiance distribution L_{scat} for a particle radius $a = 2 \cdot 10^{-6}$ m and wavelength $\lambda = 700 \cdot 10^{-9}$ m. The particle is in the center and the distribution is displayed for all directions. 0° implies forward-scattering (i.e. in the original direction) and 180° implies back-scattering (i.e. back towards the source of the light). The distribution is axially symmetric around the vector of incidence radiance.

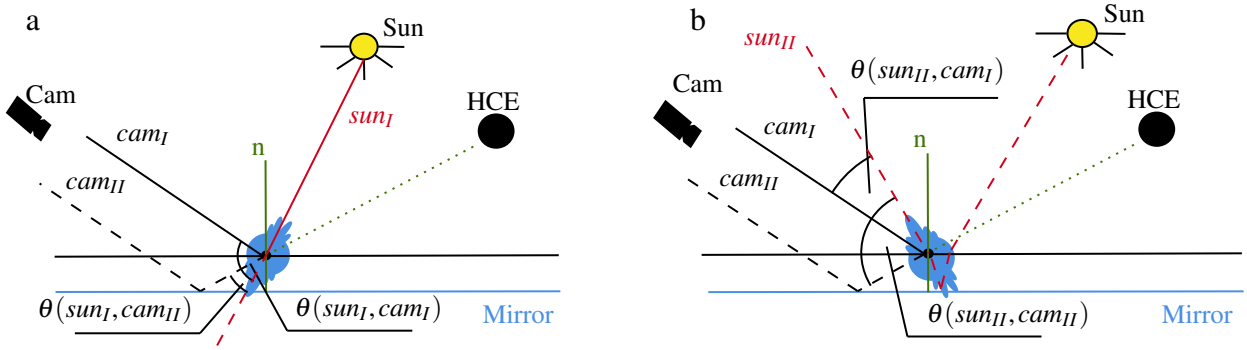

FIGURE 3. a - The sunlight is scattered directly and upon reflection at the mirror in the direction of the camera. For this reason, both contributions, cam_I and cam_{II}, shown as solid and dotted lines must be considered. **b** From the reflected sunlight, sun_{II}, two different scattering angles contributes to the camera signal.

that the phase function must be evaluated at the angle $\theta(\mathrm{sun_I}, \mathrm{cam_I})$ to obtain the radiance contribution from particle scattering in the direction of the camera.

$$L_{scat}(\theta_{\mathrm{sunI,camI}}, \varphi) = L_{sun} \cdot P(\theta_{\mathrm{sunI,camI}}, \varphi) \,, \tag{3}$$

where L_{sun} is the scattered portion of incident radiance on the particle from the direction of the sun. For clear sky conditions, L_{sun} is proportional to the direct normal irradiance (DNI) for a specific layer of spherical particles.

An analogous equation holds for $\theta(\mathrm{sun_I}, \mathrm{cam_{II}})$. The scattering cross section Q is a measure for the optically active area for a given particle. It is an output of the Mie scattering algorithm. Because the assumption of spherical particles leads to a rotation symmetric phase function, φ will be neglected in the following.

The case of scattering of solar radiation after its reflection at the mirror, i.e. incident via the vector $\mathrm{sun_{II}}$ is shown in Figure 3 b. Also here the light is scattered to the camera directly ($\mathrm{cam_I}$) and indirectly ($\mathrm{cam_{II}}$) through the mirror. Therefore, the phase function has to be evaluated at $\theta(\mathrm{sun_{II}}, \mathrm{cam_I})$ and $\theta(\mathrm{sun_{II}}, \mathrm{cam_{II}})$. This means that the method works best during clear sky conditions and that high DNI conditions are prefered. Multiple scattering is neglected, which is a good approximation for the typical range of cleanliness in operated CSP plants due to the then low particle density on the mirrors. We also neglect the contribution of scattered diffuse sky irradiance.

The scattered radiant flux, Φ_{px}^{scat}, reaching one pixel is composed of the components listed above and can be

written as

$$\Phi_{scat}^{px} = \int_{A_{Px_{cam}}} \int_{\Omega_{Px}} \Big(\quad 1 \quad \cdot L_{scat}(\theta_{\text{sunI,camI}}) \; + \\ \rho_{mirr} \quad \cdot L_{scat}(\theta_{\text{sunI,camII}}) \; + \\ \rho_{mirr} \quad \cdot L_{scat}(\theta_{\text{sunII,camI}}) \; + \\ \rho_{mirr}^2 \quad \cdot L_{scat}(\theta_{\text{sunII,camII}}) \Big) dA \; d\Omega \tag{4}$$

For the reflection at the mirror, the irradiance is attenuated by the clean mirror's reflectance ρ_{mirr}. in the last term of the equation, two reflections are involved: first the incidence sunlight is reflected, the scattered rays are reflected a second time at the mirror leading to ρ_{mirr}^2. The scattered contribution of diffuse incident radiance is neglected as its contribution to the total scattered light reaching the camera is negligible at clear sky conditions. In summary, the radiant flux incident on a pixel of the UAV camera can be written as

$$\Phi^{px} = \Phi_{scat}^{px} + \Phi_{back}^{px}. \tag{5}$$

The contributions of scattered diffuse light is neglected here. Equation 5 describes the connection between the radiation received by a pixel of the camera sensor and the cleanliness ξ.

A good understanding of the scattering processes is thus fundamental for increasing the measurement accuracy. In the following we will present the assumptions and calculations made to best estimate the scattering contribution to the irradiance incident on a camera pixel.

Scattering Simulations

The solutions of the Maxwell equations using Mie theory were calculated with the program of [17, 18]. The program is based on standard work from Bohren and Huffman [16] and publicly accessible [19]. We applied this program to calculate the scattering from a soiling layer on a CSP mirror in dependence of the particle size distribution, solar and camera sensitivity spectra and particle optical properties. A simulation framework has been built around the program to calculate all measurement scenarios from the given input data format.

Single Particle

An exemplary calculation of the scattering phase function P of a single particle will be demonstrated in this section. The input values were chosen for illustration as shown in table 1:

TABLE 1. Input Values for a Sample Calculation of the Scattering Function

$a = 2 \cdot 10^{-6}$ m	radius of the particle
$\lambda = 700 \cdot 10^{-9}$ m	wavelength of the light
$n_0 = 1.000262 + 0.000\,j$	outer medium refractive index (real)
$n_1 = 1.560000 + 0.002\,j$	particle refractive index (real + complex)
$L_{sun} = 1 \; \frac{\text{W}}{m^2 \cdot \text{sr}}$	incidence radiance that is scattered

The center of the particle is placed in the origin of the coordinate system. The diagram in Figure 2 a shows the radiance distribution function on a logarithmic scale as calculated for the above given values. Incident radiance is incident on the particle from the 180° direction, i.e. left in the diagrams.

Solar Weighting and Size Averaging

In the next step, the spectral averaging is performed to account for the influence of the normalized solar spectrum, $s(\lambda)$. Normalized meaning that the sum over all elements of the curve equals one. The averaging is performed by summing the phase function for a particle i weighted with $s(\lambda)$ over the relevant spectral range following

$$L_{scat,i}(\theta) = L_{sun,i} \cdot \sum_{\lambda_j} s(\lambda_j) \cdot P(a_i, \lambda_j, \theta) \tag{6}$$

where λ_j refers to a discrete approximation to the integration over the whole wavelength range. Two different solar spectra have been calculated using the SMARTS software [20]. The standard spectrum was calculated for air mass (AM) of 1.5 and an aerosol optical depth (AOD) of 0.084 as given also in [21]. This solar spectrum is used in the following as a standard spectrum if not stated otherwise. As a second solar spectrum more extreme conditions have been chosen with AOD = 0.5 and AM = 3 that can be referred to as hazy atmospheric conditions. In order to assess the influence of the solar spectrum on the measurement signal, the radiance distribution functions for both solar spectra are shown in Figure 4 a.

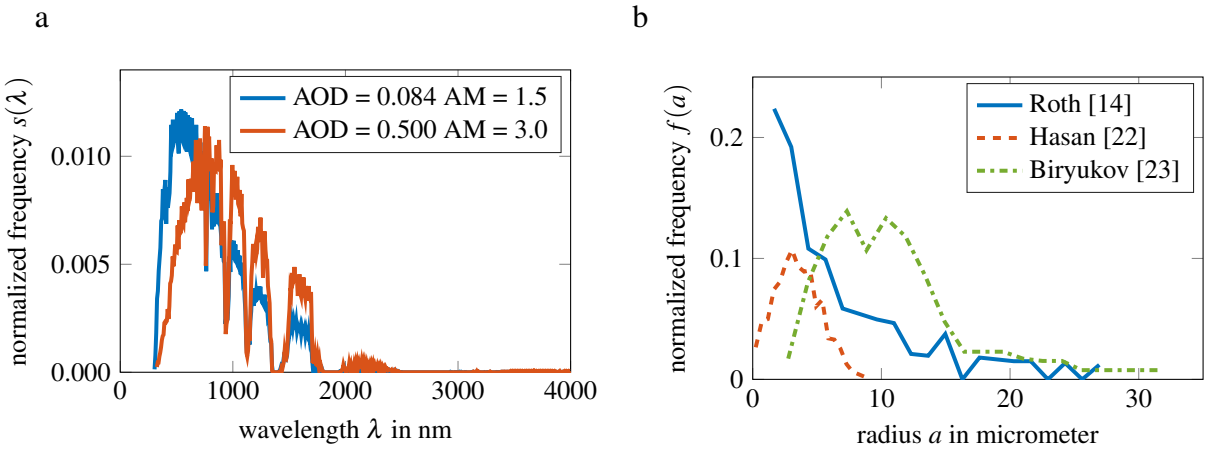

FIGURE 4. a - The solar spectra calculated with SMARTS for 2 different atmospheric conditions. **b** - Particle size distribution functions for particles that naturally deposited on glass or mirror surfaces as taken from different sources.

Particle Size Distribution

In this section we will extend the considerations made above for one particle to a particle size distribution function f. Reported size distribution functions for particles that deposited on solar surfaces during outdoor exposure have been selected for this study. They were taken from [23, 14, 22] and a normalization has been performed. the resulting size distribution functions are depicted in Figure 4 b.

With the help of the scattered light fraction per particle, $L_{\mathrm{scat,i}}$, and the normalized phase function $P(\theta)$, a function can now be calculated that represents the scattered irradiance of an entire particle size distribution constituted by N_{tot} particles with the normalized size distribution function f:

$$L_{scat}(\theta) \quad = \quad N_{tot} \sum_{i=1}^{n} f(a_i) \cdot L_{scat,i}(\theta) \tag{7}$$

where n is the number of size bins in the distribution function f. In order to derive the radiant flux incident at the camera pixel, $L_{scat}(\theta)$ has to be substituted in equation 4 and $L_{scat,i}(\theta)$ can be taken from equation 6.

The radiance functions L_{scat}^{unity} for the three size distribution functions are shown in Figure 5 a for the standard solar spectrum. The distribution of Roth is chosen as the default distribution for further calculations. If we vary the solar spectrum for that size distribution, the differences are not as significant as for changes in the particle size distribution, as can be seen in Figures 5 a and b.

Application to QFly Images

The above simulations are applied to the UAV camera's raw signals to correct for the differences in the scattering signal due to illumination, viewing and reflection angle differences. This correction will make measurement points taken at different regions within one picture or those taken from multiple images comparable. Two measurement images with the reference reflectance measurements shown as red spots are shown in Figures 6 and 7. The depicted measurement spots are used for evaluation.

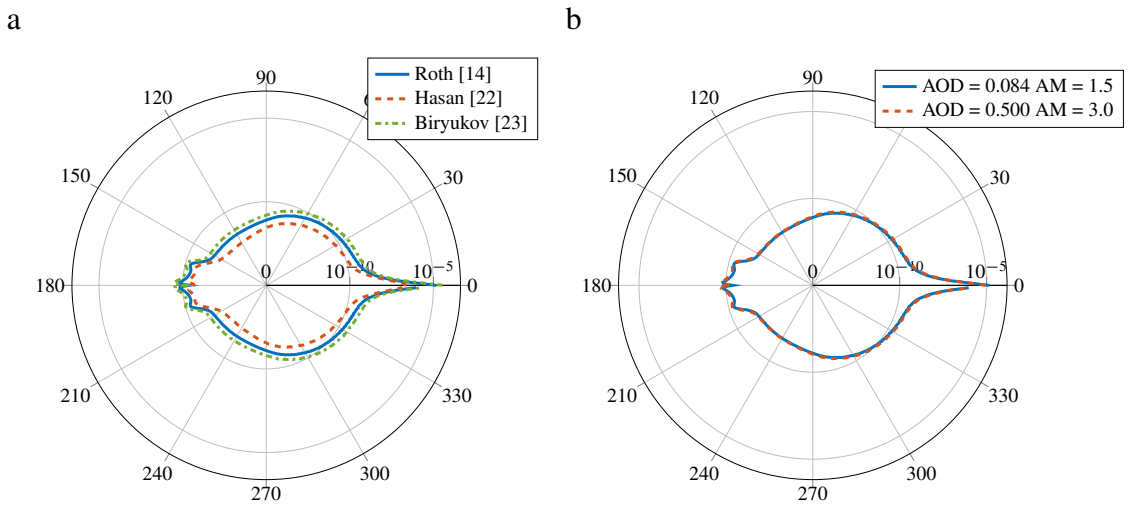

FIGURE 5. a - Simulation of the scattered radiance distribution L_{scat} calculated with equation 7 for different particle size distributions and a solar spectrum of AOD = 0.084 AM = 1.5. The distribution function of the particle size is shown in Figure 4 b. **b** - same as in a but using the particle size distribution of Roth [14] and different solar spectra. The solar spectra are shown in Figure 4 a.

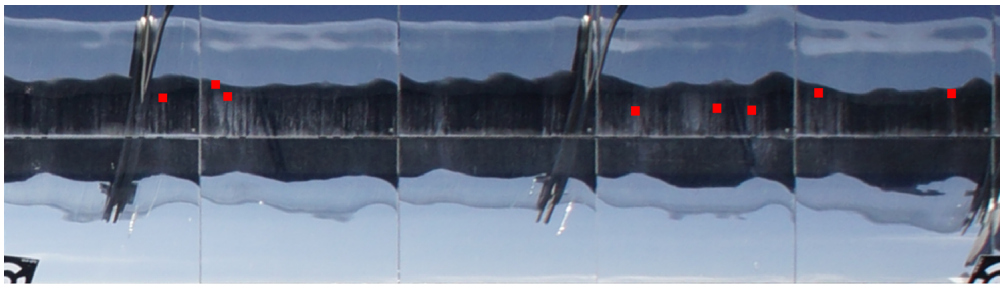

FIGURE 6. Test image 118 taken with the UAV taken after the orthogonalization. Average distance from the camera to the mirror surface is 47m.

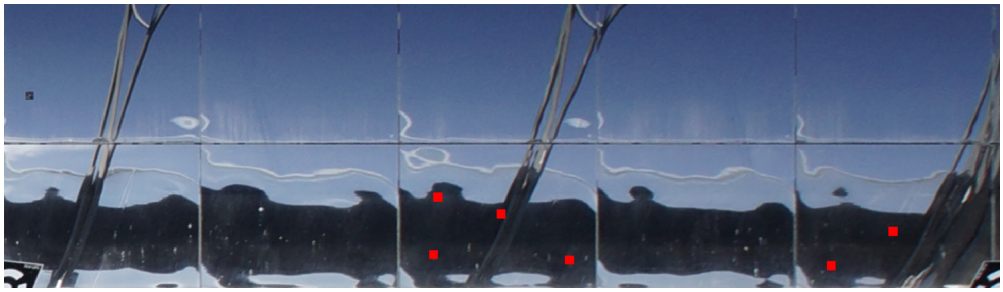

FIGURE 7. Orthoganalized test image 439 taken from an average distance of 45m from the mirror surface.

As stated above, a clear correlation can be seen if only a weighted average of the RGB values is applied to the RGB signals and plotted against the reflectance measured at the same spots. Measurement and reference measurements are fitted with a linear fit curve resulting in an R^2 of 0.49 and a RMSE of 4.7%.

In order to improve the fitting and reduce uncertainty, we correct the linearized camera RGB values, Cam^{px} by

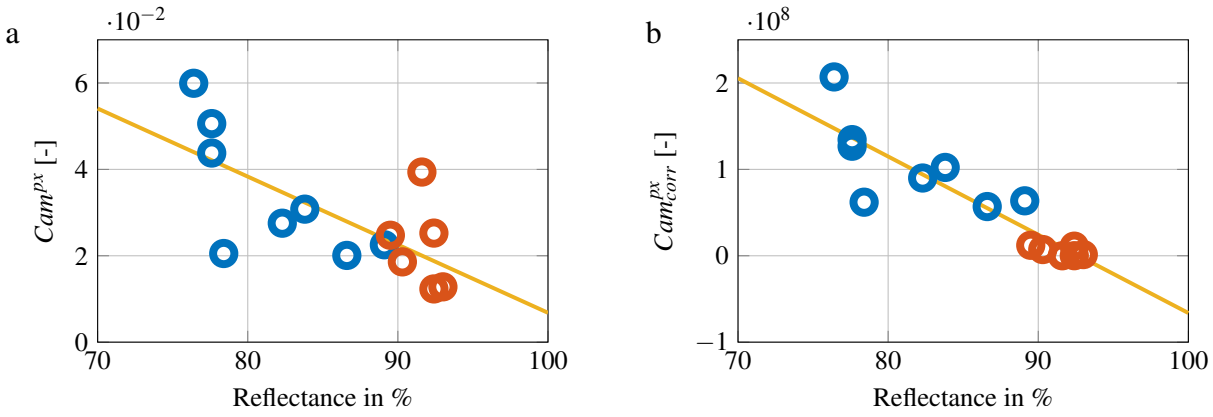

FIGURE 8. a: uncorrected weighted average of RGB signals from the reference measurement spots plotted against the reference reflectance in %. **b**: corrected RGB signal against the reference reflectance.

the directionally inhomogeneous scattering as derived above following:

$$Cam^{px}_{corr} = \frac{Cam^{px}}{\Phi^{px}_{scat}} \tag{8}$$

$$Cam^{px}_{\mathrm{BB},\perp} = (Cam^{px}_{R,corr} + Cam^{px}_{G,corr} + Cam^{px}_{B,corr})/3\,, \tag{9}$$

where "BB" stands for broadband. The background is assumed as black in this pre-study.

The correlation between a camera grey value and incoming radiation changes with the camera settings such as the aperture, the exposure time, ISO and others. Furthermore, internal modifications such as white balance and corrections to make the pictures appear more aesthetic are often applied and can make the process of deriving radiometric values from RGB signals a difficult task. Radiometric calibration has not been applied in this study and will be performed in future works.

Further, the effect of the viewing angle from the camera to the mirror needs to be considered. $Cam_{B,\perp}$ from equation 9 holds for perpendicular viewing angles. If the surface is tilted relative to the optical axis of the camera pixel, more particles move into the field of view of that pixel resulting in a higher incident radiance at a given camera pixel. The number of particles in the pixel field of view scales with the inverse of the cosine of the viewing angle. A previous study has shown that a pure cosine is not valid for cleanliness measurements on soiled mirrors due to shading and overlapping of soiling particles [24]. Before own investigations can lead to a better estimation of the cosine effect, the fit curve found in [24] is applied in this pre-study to correct for the dependency of the brightness on the camera viewing angle.

Cam_{BB} is shown in figure 8 b on the y axis against the reference reflectance of the measurement spots. The corrected RGB camera signal shows a much better correlation as the uncorrected signal. R^2 to the fit curve is 0.80 and the RMSD is 2.9% which is significantly lower than for the uncorrected camera signal.

The RMSD is the best estimate of a measurement accuracy for the proposed soiling measurement method if we assume the case of a perfect calibration of the corrected RGB signal to reflectance. Measurements with handheld reflectometers can reach an accuracy of around 1-2% reflectance [4] but they only cover a very small portion of the solar field surface. As the proposed method is capable of covering more than 95% of the solar field optical surface area, the accuracy of the average solar field cleanliness is expected to be better compared to the combined measurement and statistical error of handheld devices. The airborne method can give the additional information which parts of the field need urgent cleaning and which are cleaner than average.

Figure 8 shows that the accuracy of the method is much higher for clean mirrors than for soiled mirrors. This difference can be observed before and after the correction in Figure 8 a) and b). It can be expected that the final measuring accuracy will also behave in the same way. In the application case only reflection values up to 80% are relevant in operational power plants. For this reason the lower accuracy for highly soiled mirrors does not imply a disadvantage.

SUMMARY & OUTLOOK

A test measurement campaign has been presented that enables an airborne measurement of the soiling level of entire solar fields, e.g. during a QFly measurement campaign. The measurement principle is based solely on the camera signal, irradiance measurement and theoretical considerations on scattering distribution functions depending on particle size distributions and the solar spectrum. After correction, the camera signal correlates significantly better with the reference measurements than before the correction is applied. The RMSD for the corrected camera values is 2.9% (reflectance units) with potential for improvement if some of the assumptions made above are replaced by more sophisticated data analysis or simulation. More detailed knowledge on the background contribution can increase the correlation. Other influence factors that could be investigated in the future in order to improve the method are:

- camera radiometric calibration including vignetting effect, spectral sensitivity and color balancing
- contribution of the HCE soiling layer
- use of solar spectral measurement
- contribution of scattered diffuse irradiance

In this work, the influence of flight height has not been investigated but its limits will be tested in the future in order to find the best trade-off between minimum measurement duration and maximum resolution.

The RMSD seems high in comparison to reference handheld reflectometers that typically specify their accuracy as 1 or 2%. These instruments can only cover a very small fraction of the mirrors in a solar field. The presented method has a much higher surface coverage that can make up for eventual measurement inaccuracies. New applications in O&M procedures are possible with the presented method, especially thanks to the spatial resolution.

In summary, a novel method has been presented to measure space resolved soiling levels using a UAV. The method already delivers promising results in a test measurement campaign. The accuracy is expected to improve with further development efforts.

Acknowledgement

We thank Dr. Gueymard and Solar Consulting Services for providing the SMARTS model for this study.

REFERENCES

[1] F. Wolfertstetter, S. Wilbert, J. Dersch, S. Dieckmann, R. Pitz-Paal, and A. Ghennioui, Journal of Solar Energy Engineering **140**, p. 41008 (2018).

[2] F. Terhag, F. Wolfertstetter, S. Wilbert, T. Hirsch, and O. Schaudt, AIP Conference Proceedings **2126** (2019), 10.1063/1.5117764.

[3] F. Wolfertstetter, K. Pottler, N. Geuder, R. Affolter, A. A. Merrouni, A. Mezrhab, and R. Pitz-Paal, Energy Procedia **49**, 2422–2432 (2014).

[4] A. Fernández-García, F. Sutter, L. Martínez-Arcos, C. Sansom, F. Wolfertstetter, and C. Delord, Solar Energy Materials and Solar Cells **167**, 28–52 (2017).

[5] G. Zhu, D. Kearney, and M. Mehos, Solar Energy **99**, 185–202 (2014).

[6] J. Fernandez-Reche, Solar Energy **80**, 779–786 (2006).

[7] G. Bern, T. Schmidt, N. Celentano, A. Heimsath, and P. Nitz, "Freda-an automated field reflectance and degradation assessment system for central receiver systems," in *AIP Conference Proceedings*, Vol. 2033 (AIP Publishing, 2018) p. 230001.

[8] J. I. Zapata, C. Dally, and G. Burgess, "Estimation of average mirror reflectivity using digital photographs and specular reflectometer measurements," in *Proceedings of the 2015 Asia-Pacific Solar Research Conference, Brisbane, Australia* (2015), pp. 8–10.

[9] C. Prahl, B. Stanicki, C. Hilgert, S. Ulmer, and M. Röger, Solar Energy **91**, 68–78 (2013).

[10] P. Heller, M. Meyer-Grünefeldt, M. Ebert, N. Janotte, B. Nouri, K. Pottler, C. Prahl, W. Reinalter, and E. Zarza, SolarPACES (2011).

[11] Devices and S. Company, "Portable specular reflectometer model 15r-usb - operation and maintenance manual," Manual (2009).

[12] R. Perez, R. Seals, and J. Michalsky, Solar Energy **50**, 235–245 (1993).

[13] B. Nouri, P. Kuhn, S. Wilbert, C. Prahl, R. Pitz-Paal, P. Blanc, T. Schmidt, Z. Yasser, L. R. Santigosa, and D. Heineman, AIP Conference Proceedings **2033** (2018), 10.1063/1.5067196.
[14] E. P. Roth and A. J. Anaya, Journal of Solar Energy Engineering **102**, p. 248 (1980).
[15] H. C. v. de Hulst, *Light scattering by small particles* (Wiley, New York, 1957) p. 470.
[16] C. F. Bohren and D. R. Huffman, *Absorption and scattering of light by small particles*, 1st ed. (Wiley, New York [u.a.], 1983).
[17] J. Schaefer, S. C. Lee, and A. Kienle, Journal of Quantitative Spectroscopy and Radiative Transfer **113**, 2113–2123 (2012).
[18] J.-P. Schaefer, "Implementierung und Anwendung analytischer und numerischer Verfahren zur Loesung der Maxwellgleichungen für die Untersuchung der Lichtausbreitung in biologischem Gewebe," Ph.d. thesis, University of Ulm 2011.
[19] J.-P. Schaefer, Matscat, 2012, https://www.mathworks.com/matlabcentral/fileexchange/36831-matscat.
[20] C. Gueymard *et al.*, *SMARTS2: A Simple Model of the Atmospheric Radiative Transfer of Sunshine: Algorithms and performance assessment* (Florida Solar Energy Center Cocoa, FL, 1995).
[21] G. ASTM, Standard Tables for Reference Solar Spectral Irradiances: Direct Normal and Hemispherical on 37° Tilted Surface (2012).
[22] A. Y. Al-Hasan, Solar Energy **63**, 323–333 (1998).
[23] S. A. Biryukov, Journal of Aerosol Science **27**, p. S38 (1996).
[24] A. Heimsath, P. Lindner, E. Klimm, T. Schmid, K. O. Moreno, Y. Elon, M. Am-Shallem, and P. Nitz, "Specular reflectance of soiled glass mirrors–study on the impact of incidence angles," in *AIP Conference Proceedings*, Vol. 1734 (AIP Publishing, 2016) p. 130009.
[25] F. Wolfertstetter, K. Pottler, A. A. Merrouni, A. Mezrhab, and R. Pitz-Paal, "A novel method for automatic real-time monitoring of mirror soiling rates," in *18th Solar Paces International Symposium, Marrakesh, Morocco* (2012).
[26] E. Berra, S. Gibson-Poole, A. MacArthur, R. Gaulton, and A. Hamilton, International Archives of the Photogrammetry, Remote Sensing & Spatial Information Sciences **40** (2015).
[27] S. Wilbert, B. Reinhardt, J. DeVore, M. Röger, R. Pitz-Paal, C. Gueymard, and R. Buras, Journal of Solar Energy Engineering **135**, p. 41002 (2013).